Proceedings of the Canadian Society for Mechanical Engineering International Congress
32nd Annual Conference of the Computational Fluid Dynamics Society of Canada
Canadian Society of Rheology Symposium
CSME/CFDSC/CSR 2025
May 25–28, 2025, Montréal, Québec, Canada

Exploring Miscible Jet Dynamics in Complex Fluids

Hossein Hassanzadeh[1,2], Mariana Cruz Banda[1], Seyed Mohammad Taghavi[1*]

[1]Department of Chemical Engineering, Université Laval, Québec, QC, Canada
[2]Department of Mechanical Engineering, University of British Columbia, Vancouver, BC, Canada
[*]seyed-mohammad.taghavi@gch.ulaval.ca

***Abstract*—**This study explores the fluid dynamics of a Newtonian jet injected horizontally into a viscoplastic (yield stress) ambient fluid, a process relevant to various industrial applications, including jet cleaning process in oil and gas wells. To replicate industrial scenario, a perforated wall is considered between the nozzle and the tank wall, dividing the flow domain into two zones. We focus on the effects of key parameters, including the perforation diameter and the rheological properties of the ambient fluid, on jet behavior. The jet radius is used as a main metric to quantify mixing, while self-similarity is examined across varying conditions to provide insights into jet dynamics. The results reveal that a reduction in the perforation diameter leads to an increase in jet radius in the first zone, while causing a decrease in the second zone. In addition, the jet maintains its self-similar behavior, regardless of the perforation size. Furthermore, the presence of a viscoplastic fluid contributes to a decrease in the jet radius in both zones and deviate from self-similarity behavior, highlighting the significant impact of yield stress on the jet flow dynamics. These findings provide valuable insights into jet flow and can be leveraged to optimize jet cleaning processes, with the dimensionless results allowing for their extension to a range of relevant applications involving jets and non-Newtonian fluids, including liquid-in-liquid printing, cleaning-in-place systems, and industrial mixing operations.

***Keywords*—Jets; Viscoplastic fluids; self-similarity; yield stress; cleaning**

I. INTRODUCTION

Jet flow is a phenomenon where a fluid is forced through a small opening (i.e., nozzle) into another fluid [1]. These flows are found in numerous natural processes and engineering applications. For example, jet flows are pivotal in operations, including 3D printing, drug delivery, mixing, cleaning, and cooling [1]–[3]. In nature, jet flows contribute to phenomena such as cloud movement and play a key role in geological activities like geysers, fumaroles, and volcanic eruptions [1]. While jet flows often involve non-Newtonian fluids in many contexts, the majority of research has focused around Newtonian fluids, leaving a gap in the understanding of jet flows interacting with non-Newtonian fluids, particularly viscoplastic fluids. This knowledge gap serves as the motivation for the present study, which aims to deepen our understanding of jet flow behavior in such fluids from a fundamental perspective.

The main motivation of this study is to assess cleaning processes in plug and abandonment (P&A) operations for oil and gas wells. When a well reaches the end of its productive life and the remaining hydrocarbons are no longer economically viable, it must be plugged and abandoned [4], [5]. This process is essential to prevent environmental hazards such as hydrocarbon leakage into adjacent layers, contamination of water-bearing zones, and gas emissions into the atmosphere [6]. A key aspect of P&A operations is the creation of a reliable seal, typically achieved through a cement plug that prevents fluid migration. However, the success of the seal relies on effective cleaning of the target area. Poor cleaning can lead to cement contamination, compromising the integrity of the plug and potentially causing P&A failure [7], [8]. Jet cleaning, a relatively new technology, has proven to be an efficient method for cleaning the target area. By injecting a fluid to form a high-velocity jet, unwanted materials are displaced, preparing the well for the cementing process. The efficiency of the jet cleaning depends on several factors, including fluid properties and geometrical parameters. For instance, the unwanted fluid to be displaced typically exhibits yield stress behavior. Understanding the dynamics of jet flow is therefore critical to enhancing the cleaning efficiency and ensuring the success of the P&A operation.

A non-buoyant jet, or pure jet, is formed when a fluid is injected from a nozzle into an ambient fluid of the same density, driven by the source momentum [1], [9]. Jets can be generally categorized into two types—miscible and immiscible—depending on the role of interfacial tension [10].

This study focuses on non-buoyant miscible jets, where the interfacial tension effect is assumed to be negligible. The Reynolds number, Re, is a key parameter that governs the flow behavior of miscible non-buoyant jets, as it represents the ratio of inertial forces to viscous forces. Research has shown that variations in the Reynolds number significantly affect jet characteristics. One of the main jet characteristics is the jet radius, which serves as a representative feature for the mixing behavior. As the jet moves away from the nozzle, its radius increases due to the mixing process, where the ambient fluid is drawn into the jet [11]. Several studies have explored how the jet radius changes with different parameters. As demonstrated by Hassanzadeh et al. [12], the jet radius slightly decreases with an increase in the Reynolds number. Also, the literature suggests that higher jet density and increased viscosity of the ambient fluid both contribute to a reduction in the jet radius [13], [14].

Non-Newtonian fluids, especially those exhibiting yield stress, are commonly found in many industrial applications, including P&A operations. To describe the rheological behavior of these fluids, the Herschel-Bulkley model is widely used due to its ability to account for both the yield stress and the shear-thinning behavior [1], which are characteristic of such fluids. The model is formulated as:

$$\hat{\tau} = \hat{\tau}_y + \hat{\kappa} \left(\frac{\hat{V}_0}{\hat{D}_n} \right)^n, \tag{1}$$

where $\hat{\tau}_y$, $\hat{\kappa}$, $\hat{V}_0$, $\hat{D}_n$, and n represent the yield stress, consistency, injection velocity, nozzle diameter, and power-law index, respectively. In this paper, dimensional quantities are represented with the "$\hat{}$" symbol, whereas dimensionless quantities are shown without it.

The Bingham number, B_N, is a dimensionless parameter that characterizes the effect of viscoplastic properties on fluid flow, given by:

$$B_N = \frac{\hat{\tau}_y \hat{D}_n}{\hat{\mu}_j \hat{V}_0}. \tag{2}$$

Here, $\hat{\mu}_j$ is the viscosity of the jet fluid. This number highlights the balance between the yield stress of the ambient fluid and the viscous forces of the injected fluid.

There is limited research on the influence of viscoplastic fluids on jet flow behavior. Kumar et al. [15] investigated the effects of the Reynolds and Bingham numbers on viscoplastic jet dynamics. They found that in certain Reynolds number ranges, the Bingham number has minimal impact, with turbulent forces dominating. However, in lower Reynolds numbers, both Re and B_N significantly influence jet flow behavior. Hassanzadeh et al. [16] investigated the behavior of injecting a Newtonian fluid into a viscoplastic ambient fluid, identifying various flow regimes. Their findings showed that increasing the Bingham number results in significant changes to the jet dynamics, particularly a decrease in jet velocity. Recently, Moosavi et al. [17] conducted an experimental study on a horizontal buoyant jet by injecting a dense Newtonian fluid into a lighter viscoplastic ambient fluid. They observed a significant reduction in the jet area as the viscosity ratio between the fluids increased.

This work provides novel insights into the dynamics of non-buoyant miscible jets, specifically in the context of jet cleaning during P&A operations. By conducting experimental analyses, we examine the impact of key parameters, such as the geometrical parameter (i.e., perforation diameter) and the presence of viscoplastic fluids (quantified by the Bingham number), on jet behavior. Our findings provide a deeper understanding of the complex fluid dynamics involved, contributing to enhanced cleaning efficiency and optimization of P&A operations.

This paper is structured as follows: The next section outlines an overview of the experimental setup, procedures, and methodologies employed to capture and analyze the jet flow behavior. Next, the general characteristics and behavior of non-buoyant miscible horizontal jets are presented. We then explore how the perforation diameter and the Bingham number influence jet dynamics. Finally, we conclude by summarizing the key findings and insights gained from the study.

II. Experiments

A schematic of the experimental setup is shown in Fig. 1. The experiments were performed in a transparent rectangular tank, where a perforated wall separated the domain into two zones. The perforated wall, placed between the injection nozzle and the end-wall of the tank, mimicked the real-world scenario of a perforated casing in the gap between jetting tools and the formation wall. The perforated wall contained five holes of identical diameter, arranged evenly, with the central hole aligned with the nozzle's center. The two zones were interconnected through these holes. In the experiment, miscible horizontal jets were generated by injecting deionized water, driven by an ISMATEC MCP-Z Standard gear pump, horizontally through a cylindrical nozzle into the tank containing a miscible ambient fluid. The nozzle was located at the center of the tank's wall. To enhance visibility, the injected fluid was colored with ink, and it first passed through the initial zone before entering the second zone via the perforations in the wall.

In most of the experiments, deionized water was used as the main working fluid. The key parameters varied during the study included the injection velocity, the size of the perforation holes, and the type of ambient fluid. All other parameters, including the nozzle diameter, nozzle-to-wall distance, and fluid densities, remained constant during the experiments. A high-precision pump was used to cover a broad range of Reynolds numbers, with values ranging from $2000 < Re = \frac{\hat{\rho}_j \hat{V}_0 \hat{D}_n}{\hat{\mu}_j} < 10000$, corresponding to varying injection velocities. To assess the effect of the ambient fluid properties, experiments were performed using both Newtonian fluids, where $B_N = 0$, and non-Newtonian fluids, for which $0 < B_N < 45$. To prepare the non-Newtonian fluid, Carbopol gel was chosen for its transparency and low toxicity. The preparation involved first mixing the Carbopol powder (Carbomer 940, Making Cosmetics Co.) with

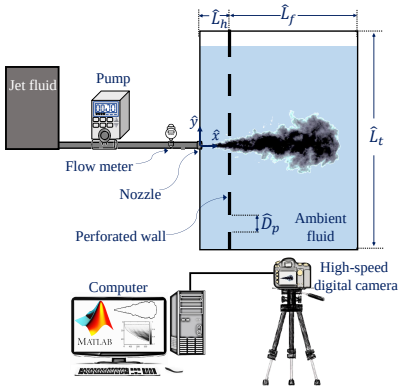

Figure. 1: Schematic view of our experimental setup. The main measurement technique is grayscale image analysis. Key dimensions (normalized by $\hat{D}_n$): $L_h = 8.3$, $L_f = 28$, $L_t = 83$, $D_p = 0.5$–5.6.

deionized water to form an acidic solution. Following this, sodium hydroxide was added to neutralize the pH, resulting in a gel with a yield stress that maintained a density comparable to deionized water. A digital rheometer (DHR-3, TA Instruments) was employed to determine gel's rheological characteristics. Note that, since buoyancy forces have a negligible effect on non-buoyant jets (i.e., when $\hat{\rho}_j = \hat{\rho}_a$), the insights gained from this study are relevant to understanding the behavior of both horizontal and vertical jets.

In this work, jet flow behavior was captured through direct visualization, allowing for the analysis of large-scale features, like the jet radius via quantitative image processing. To improve contrast and facilitate visualization, black ink was mixed into the injected fluid. The rectangular tank used in the experiment was uniformly illuminated by LED light boxes placed on the top, sides, and back, with diffusers ensuring consistent lighting across the entire tank. A high-speed digital camera, the Basler aca2040-90um, was employed to capture images of the jet behavior, typically at 50 frames per second with a 4 MP resolution. The captured images were then processed using custom MATLAB code to convert the light intensity values into normalized concentration profiles averaged across the depth of the tank.

III. RESULTS AND DISCUSSION

This section begins with an overview of our key observations related to the jet flow dynamics. Following this, we investigate the influence of the perforation diameter, D_p, and the Bingham number, B_N, on the behavior of miscible horizontal jets.

A. General observation

Fig. 2a presents a typical horizontal jet, where a dyed jet fluid is injected into a tank filled with transparent deionized water. The flow domain is divided into two zones by a perforated wall: (I) the first zone, extending from the nozzle to the perforated wall, and (II) the second zone, located beyond the perforated wall. As the injected fluid enters the first zone, it begins to mix with the ambient fluid before passing through the perforation and continuing into the second zone. The intensity of mixing increases progressively as the jet moves further from the nozzle, as indicated by the darker areas. Finally, the jet reaches the end-wall, where its direction shifts from longitudinal to transverse. Note that, throughout the paper, we make the length, velocity, and time dimensionless by normalizing them with $\hat{D}_n$, $\hat{V}_{j,0}$, and $\frac{\hat{D}_n}{\hat{V}_{j,0}}$, respectively.

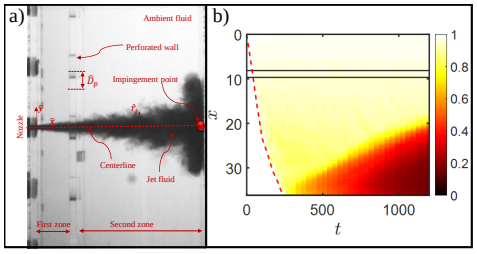

Figure. 2: (a) A typical horizontal jet observed in our experiments. The red dashed line marks the jet centerline, passing through the center of both nozzle and hole. The jet radius, $\hat{r}_j$, quantifies the transverse growth of the jet. The red point indicates the impingement point, where the jet axis intersects the impingement wall. (b) Spatiotemporal diagram of depth-averaged concentration profiles in the $x-t$ plane corresponding to the experiment in (a). The solid black lines mark the perforated wall, which separates the experimental domain into two main zones. The red dashed line indicates the leading front of the jet.

The evolution of jet flow behavior can be observed in the spatiotemporal concentration diagram in Fig. 2b. This diagram presents the concentration profile along the axial length of the tank (x-direction), averaged over the width (y- and z-directions). The color gradient spans from 0 (representing pure jet fluid) to 1 (indicating pure ambient fluid), with intermediate values reflecting varying degrees of mixing at different spatial and temporal points. As shown in Fig. 2b, the mixing between the jet and ambient fluid begins immediately upon injection ($x = 0$, $t = 0$) and intensifies over time and distance, indicated by the progressive decrease in normalized concentration values. Upon reaching the end-wall ($x \approx 36$), the backflow is generated, further enhancing the mixing. This phenomenon is particularly visible in Fig. 2b, where the intensified color region signifies the enhanced mixing occurring after impingement.

B. Effects of perforation diameter (D_p)

To optimize the jet cleaning process, it is important to understand how geometrical parameters impact the flow behavior. This section examines the influence of the dimensionless perforation diameter, denoted as $D_p = \hat{D}_p/\hat{D}_n$, where $\hat{D}_p$ and $\hat{D}_n$ represent the perforation and nozzle diameters, respectively, on the jet behavior. By exploring the perforation diameter in its dimensionless form, the results obtained can be applied to a range of conditions involving varying nozzle or perforation sizes.

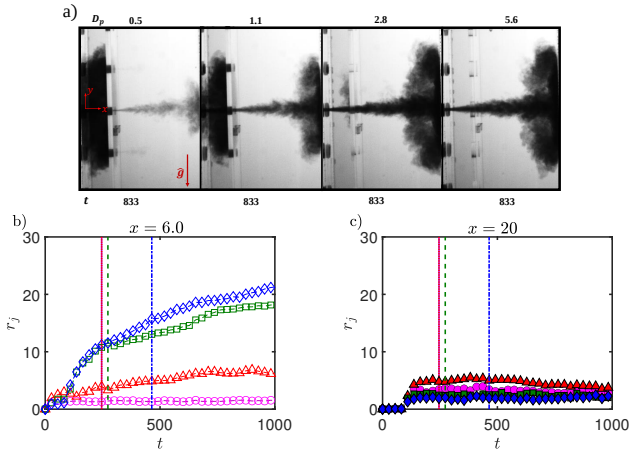

Figure. 3: (a) Snapshots of horizontal jets with varying perforation diameters (i.e., $D_p = \hat{D}_p/\hat{D}_n$): from left to right $D_p = 0.5$, $D_p = 1.1$, $D_p = 2.8$, $D_p = 5.6$. The dimensionless times are indicated below each snapshot. (b) and (c) Temporal evolution of the dimensionless jet radius at different axial positions: (b) $x = 6.0$ and (c) $x = 20.0$. The symbols represent the following perforation diameters: $D_p = 0.5$ (blue diamond), $D_p = 1.1$ (green square), $D_p = 2.8$ (red triangle), and $D_p = 5.6$ (pink circle). The vertical lines indicate the impingement times for the corresponding experiments, matched with the same color as the symbols. In all subfigures, the other experimental parameters remain constant, with $Re \approx 7100$ and $B_N = 0$.

Fig. 3a presents a series of snapshots showing the behavior of the horizontal jet at different perforation diameters, revealing distinct changes in jet dynamics. With a constant Reynolds number ($Re \approx 7100$) and for Newtonian cases ($B_N = 0$), a reduction in perforation diameter leads to increased mixing in the first zone. This effect starts to appear at $D_p = 2.8$, as seen in the third snapshot of Fig. 3a, where the interaction between the jet and the perforation wall promotes additional mixing in the first zone. In contrast, for $D_p = 5.6$ (shown in the last snapshot of Fig. 3a), the perforated wall has a minimal effect on the jet behavior. When the perforation diameter is nearly equal to the nozzle diameter ($\hat{D}_p \approx \hat{D}_n$; $D_p = 1.1$), strong mixing between the jet and the ambient fluid occurs in the first zone, as demonstrated in the second snapshot of Fig. 3a. For the smallest perforation diameter ($D_p = 0.5$), depicted in the first snapshot in Fig. 3a, the mixing is strongest in the first zone, however, this is accompanied by a smaller and weaker jet in the second zone. It is important to note that the injection fluid volume remains consistent across all experiments.

For a quantitative comparison, the temporal evolution of the jet radius at two axial positions is presented in Fig. 3b (at $x = 6.0$, in the first zone) and Fig. 3c (at $x = 20.0$, in the second zone). Note that, the jet radius refers to half the width of the jet observed from the side view at specific axial positions. The vertical lines mark the impingement time for each experiment, with corresponding colors. In the first zone (Fig. 3b), the jet radius increases as the perforation diameter decreases, with the largest radius occurring at $D_p = 0.5$. In the case of $D_p = 5.6$, where the interaction between the jet and the perforated wall is minimal, the jet radius in the first zone is the smallest. Moreover, decreasing the perforation diameter results in the jet requiring more time to reach the end-wall, with the jet having the smallest perforation diameter taking the longest to impinge. At $x = 20.0$ (in the second zone), as shown in Fig. 3c, decreasing the perforation diameter generally leads to a reduction in the jet radius, indicating that the jet becomes smaller and the mixing diminishes in the second zone. Furthermore, in all cases except for $D_p = 5.6$, the jet radius in the second zone is smaller than that in the first zone. For $D_p = 5.6$, however, the jet radius at $x = 20.0$ exceeds that at $x = 6.0$, consistent with observations in the literature [12], [18], where the jet radius is known to increase with axial distance.

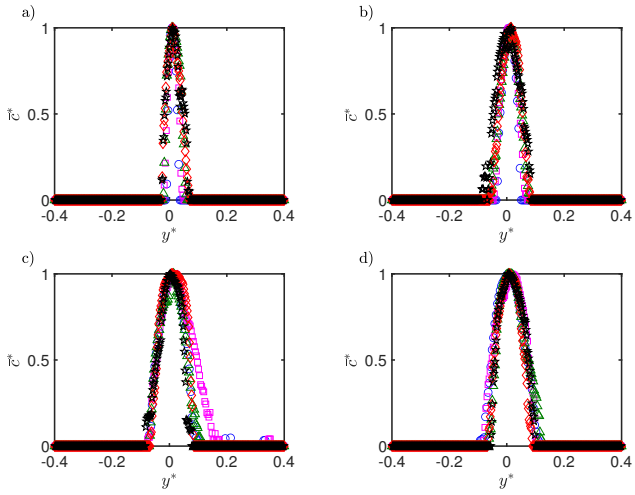

Figure. 4: Variation of $\bar{c}^* = \bar{c}/c_{max}$ versus $y^* = y/x$ for (a) $D_p = 0.5$, (b) $D_p = 1.1$, (c) $D_p = 2.8$, (d) $D_p = 5.6$. All other experimental parameters remain constant, with $Re \approx 7100$ and $B_N = 0$. Each subfigure shows data at different axial positions, with the symbols representing: $x = 14$ (blue circle), $x = 18$ (pink square), $x = 22$ (green triangle), $x = 26$ (red diamond), and $x = 30$ (black star).

Self-similarity is a key principle in fluid mechanics [19], referring to the consistent scaling of flow characteristics across different spatial and temporal scales. In jet flows, this concept is particularly useful as it predicts the evolution of flow features as the jet progresses downstream. Through self-similarity, data from multiple positions can be collapsed into a single, unified framework, highlighting the fundamental, universal behaviors of the flow. Now, we explore the self-similarity of concentration profiles to further understand the dynamics of jet flows.

To analyze the self-similarity of concentration profiles, we normalize the mean concentration by its maximum value at each axial position, defined as:

$$\bar{c}^* = \bar{c}/c_{\max}, \tag{3}$$

where $c_{\max}$ is the maximum concentration at certain axial position. The transverse direction (y) is scaled by the axial distance, using

$$y^* = y/x. \tag{4}$$

For visualization purposes, the concentration is transformed as $\bar{c} = 1 - \bar{c}$. Fig. 4a-d present the variation of $\bar{c}^*$ with y^* at different axial positions for $D_p = 0.5$, 1.1, 2.8, and 5.6, respectively. The data points from five distinct axial positions nearly collapse onto a single curve for all perforation diameters, indicating that the jet flow in the second zone exhibits self-similar behavior, regardless of the perforation diameter. However, an interesting trend is observed: as D_p increases from 0.5 to 5.6 (from subfigure a to d), the region of none-zero self-similarity broadens. This indicates that smaller perforation diameters can significantly reduce mixing and weaken the jet's ability to entrain the ambient fluid.

C. *Effects of viscoplasticity (B_N)*

The interaction between the jet and ambient fluids is significantly influenced by their rheological properties. To examine the role of viscoplasticity, we analyze jet flow behavior at varying Bingham numbers while maintaining a constant Reynolds number ($Re \approx 3000$) and a perforation diameter ($D_p = 5.6$), as illustrated in Fig. 5a. A clear distinction occurs between Newtonian ($B_N = 0$) and non-Newtonian ($B_N \neq 0$) ambient fluids. In the Newtonian case (first snapshot in Fig. 5a), obvious mixing occurs at the jet boundaries. However, when the ambient fluid exhibits small viscoplasticity (second snapshot in Fig. 5a), this mixing at the jet boundary is reduced. The yield stress suppresses small-scale perturbations, stabilizing the jet interface and limiting entrainment. Moreover, the backflow behavior differs between these cases, further emphasizing the influence of viscoplasticity. As the Bingham number increases, the jet undergoes a fundamental transition, as evident from Fig. 5b to c. At the high yield stress fluid, the jet fails to reach the end-wall within the observed time scale, and instead, multiple finger-like structures appear at its boundary, ranging from small to large scales. This behavior suggests that the resistance imposed by the ambient fluid surpasses the jet's inertial forces, causing a notable change in mixing behavior and highlighting the important role of viscoplasticity in controlling jet dynamics and flow evolution.

The evolution of the jet radius over time at two different axial positions is plotted in Fig. 5b (at $x = 6.0$, in the first zone) and Fig. 5c (at $x = 20.0$, in the second zone). In the first zone (Fig. 5b), as the Bingham number increases, the jet radius slightly decreases. While increasing the Bingham number from 0 to 0.4 does not significantly affect the impingement time, the case with $B_N = 43.1$ results in impingement occurring much later, around $t \approx 2300$, outside the shown time range. In the second zone ($x = 20.0$), as shown in Fig. 5c, the jet radius generally decreases with increasing Bingham number. A closer look reveals two key observations: first, the jet reaches $x = 20$ more slowly for $B_N = 43.1$ compared to the other cases. Second, the jet radius remains nearly constant over time for $B_N = 0.0$ and $B_N = 0.4$, whereas for $B_N = 43.1$, the jet radius gradually increases over time, showing the transient nature of jet flow in the presence of high yield stress fluids. Note that the sudden increase at the last part of $B_N = 0.0$ is due to backflow.

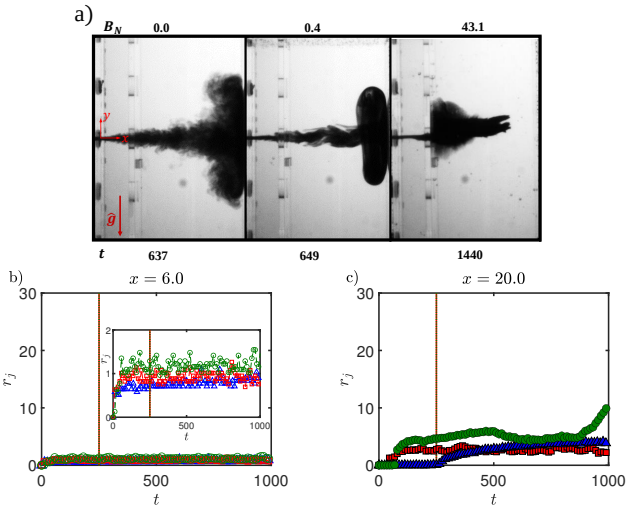

Figure. 5: (a) Snapshots of horizontal jets with different Bingham numbers (B_N), arranged from left to right: $B_N = 0.0$, $B_N = 0.4$, and $B_N = 43.1$. The dimensionless times are indicated below each snapshot. (b) and (c) Variation of the dimensionless jet radius versus time at different axial positions: (b) at $x = 6.0$ and (c) at $x = 20.0$. The symbols correspond to the following B_N values: $B_N = 0.0$ (green circle), $B_N = 0.4$ (red square), and $B_N = 43.1$ (blue triangle). Vertical lines indicate the impingement times for the corresponding experiments, with colors matching the symbols. Note that the impingement times for $B_N = 0.0$ 0.4 are nearly identical (their lines overlap), while the impingement time for $B_N = 43.1$ occurs beyond the observable range ($t \approx 2300$). The inset in subfigure (b) shows a zoomed-in view of the main plot, focusing on a smaller range of r_j ($0 \leq r_j \leq 2$). All other experimental parameters are consistent across all subfigures, with $Re \approx 3000$ and $D_p = 5.6$.

Fig. 6a-c show the variation of $\bar{c}^*$ versus y^* at five different axial positions for $B_N = 0.0$, 0.4, and 43.1, respectively. In Fig. 6a, the jet exhibits strong self-similarity, with all data points collapsing onto a single curve, suggesting that the jet's behavior can be reliably predicted both spatially and temporally. As the Bingham number increases, the concentration profile starts to deviate from this self-similar pattern. For $B_N = 0.4$, the deviation is minor, and the profile remains relatively consistent. However, at $B_N = 43.1$ (Fig. 6c), the data points no longer follow a single curve, indicating a transition to transient behavior in both space and time. This observation is consistent with our previous findings and further emphasizes the significant role of viscoplasticity in changing the jet flow dynamics.

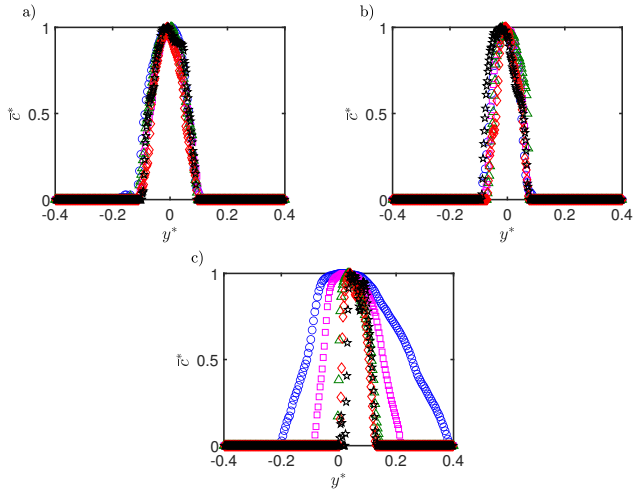

Figure. 6: Variation of $\bar{c}^*$ with respect to y^* for (a) $B_N = 0.0$, (b) $B_N = 0.4$, and (c) $B_N = 43.1$. All cases at $Re \approx 3000$ and $D_p = 5.6$. Each subfigure presents data for different axial positions, with the following symbols: $x = 14$ (blue circle), $x = 18$ (pink square), $x = 22$ (green triangle), $x = 26$ (red diamond), and $x = 30$ (black star).

IV. CONCLUSION

This study delved into the fluid dynamics of jetting, particularly focusing on its role in cleaning processes during P&A operations. The experimental setup involved horizontally injecting a jet fluid into a transparent rectangular tank filled with an ambient fluid. Both fluids were miscible and had identical densities ($\hat{\rho}_j = \hat{\rho}_a$), allowing the results to be applicable to both horizontal and vertical jet configurations. A perforated wall was included in the tank design to divide it into two zones, mimicking P&A cleaning processes.

The main objective was to assess the influence of key parameters, including the perforation diameter and the rheological properties of the ambient fluid, on the jet flow behavior. The findings were analyzed using relevant dimensionless numbers to generalize the results. The jet radius, defined to quantify the mixing behavior, exhibited an increase in the first zone with a smaller perforation diameter (D_p), whereas in the second zone, it showed a reduction. Moreover, when the ambient fluid exhibited non-Newtonian behavior (i.e., $B_N \neq 0$), the jet radius was reduced in both zones. The study also investigated the self-similarity of the concentration profile. While the perforation diameter had minimal effect on the self-similar behavior, an increase in the Bingham number caused a deviation from self-similarity, indicating that higher yield stress fluids introduced greater complexity into the jet flow dynamics.

ACKNOWLEDGMENT

This research was conducted at Université Laval. The authors acknowledge financial support from PTAC-AUPRF (Grant No. AUPRF2022-000124) and NSERC Alliance (Grant No. ALLRP577111-22) for the project Towards Net-Zero Emissions, as well as the Canada Research Chair in Modeling Complex Flows (Grant No. CG125810), the Canada Foundation for Innovation (Grants No. GF130120, GQ130119, and GF525075), and NSERC through the Discovery Grant (Grant No. CG109154) and Research Tools and Instruments Grant (Grant No. CG132931). HH gratefully acknowledges the ENVOL-FSG scholarship. Special thanks to J. Noël and J.N. Ouellet, departmental technicians at Université Laval, for their invaluable assistance in constructing the experimental setup and their insightful technical discussions.

REFERENCES

[1] Hassanzadeh, H., and Taghavi, S. M., 2024. "A review on free miscible buoyant jets". *Physics of Fluids,* ***36***(6).

[2] Rosselló, J. M., and Ohl, C. D., 2022. "Bullet jet as a tool for soft matter piercing and needle-free liquid injection". *Biomedical Optics Express,* ***13***(10), pp. 5202–5211.

[3] Hassanzadeh, H.and Wilson, D. I., Frigaard, I. A., and Taghavi, S. M., 2024. "Turbulent impingement jet cleaning of thick viscoplastic layers". *Journal of Non-Newtonian Fluid Mechanics*, p. 105264.

[4] Khalifeh, M., and Saasen, A., 2020. *Introduction to permanent plug and abandonment of wells*. Springer Nature.

[5] Hassanzadeh, H., Joshi, S., Akbari, S., and Taghavi, S. M., 2023. "Buoyant miscible jets in a viscoplastic medium with applications in plug and abandonment of oil and gas wells". In International Conference on Offshore Mechanics and Arctic Engineering, Vol. 86915, American Society of Mechanical Engineers, p. V009T11A030.

[6] Opara, S. U., and Okere, C. J., 2024. "A review of methane leakage from abandoned oil and gas wells: A case study in Lubbock, Texas, within the Permian Basin". *Energy Geoscience*, p. 100288.

[7] Vrålstad, T., Saasen, A., Fjær, E., Øia, T., Ytrehus, J. D., and Khalifeh, M., 2019. "Plug & abandonment of offshore wells: Ensuring long-term well integrity and cost-efficiency". *Journal of Petroleum Science and Engineering,* ***173***, pp. 478–491.

[8] Hassanzadeh, H., Eslami, A., and Taghavi, S. M., 2021. "Buoyant miscible jets in the plug and abandonment of oil and gas wells". In International Conference on Offshore Mechanics and Arctic Engineering, Vol. 85208, American Society of Mechanical Engineers, p. V010T11A055.

[9] Fischer, H. B., List, J. E., Koh, C. R., Imberger, J., and Brooks, N. H., 2013. *Mixing in inland and coastal waters*. Elsevier.

[10] Eslami, A., and Taghavi, S. M., 2020. "Viscoplastic fingering in rectangular channels". *Physical Review E,* ***102***(2), p. 023105.

[11] Sreenivas, K. R., and Prasad, A. K., 2000. "Vortex-dynamics model for entrainment in jets and plumes". *Physics of Fluids,* ***12***(8), pp. 2101–2107.

[12] Hassanzadeh, H., Eslami, A., and Taghavi, S., 2021. "Positively buoyant jets: semiturbulent to fully turbulent regimes". *Physical Review Fluids,* ***6***(5), p. 054501.

[13] Hassanzadeh, H., Joshi, S., and Taghavi, S. M., 2023. "Predicting buoyant jet characteristics: a machine learning approach". *Chemical Product and Process Modeling*(1).

[14] Hassanzadeh, H., Eslami, A., and Taghavi, S., 2022. "On the role of the viscosity ratio on buoyant miscible jet flows". *Environmental Fluid Mechanics,* ***22***(2-3), pp. 337–365.

[15] Kumar, K. R., Rankin, G. W., and Shidhar, K., 1984. "Laminar length of a non-Newtonian fluid jet". *Journal of non-Newtonian Fluid Mechanics,* ***15***(1), pp. 13–27.

[16] Hassanzadeh, H., Frigaard, I., and Taghavi, S., 2023. "Neutrally buoyant miscible jets into viscoplastic ambient fluids". *Journal of Non-Newtonian Fluid Mechanics,* ***320***, p. 105107.

[17] Moosavi, M. H., Hassanzadeh, H., and Taghavi, S. M., 2024. "Horizontal buoyant jets into viscoplastic ambient fluids". *Applications in Engineering Science,* ***20***, p. 100192.

[18] Bhamidipati, N., and Woods, A. W., 2017. "On the dynamics of starting plumes". *Journal of Fluid Mechanics,* ***833***, p. R2.

[19] Gratton, J., 1991. "Similarity and self similarity in fluid dynamics". *Fundamentals of Cosmic Physics,* ***15***, pp. 1–106.